Water-Lubricated Intercalation in $V_2O_5 \cdot nH_2O$ for High-Capacity and High-Rate Aqueous Rechargeable Zinc Batteries

Mengyu Yan, Pan He, Ying Chen, Shanyu Wang, Qiulong Wei, Kangning Zhao, Xu Xu, Qinyou An, Yi Shuang, Yuyan Shao, Karl T. Mueller, Liqiang Mai,* Jun Liu, and Jihui Yang*

Low-cost, environment-friendly aqueous Zn batteries have great potential for large-scale energy storage, but the intercalation of zinc ions in the cathode materials is challenging and complex. Herein, the critical role of structural H_2O on Zn^{2+} intercalation into bilayer $V_2O_5 \cdot nH_2O$ is demonstrated. The results suggest that the H_2O-solvated Zn^{2+} possesses largely reduced effective charge and thus reduced electrostatic interactions with the V_2O_5 framework, effectively promoting its diffusion. Benefited from the "lubricating" effect, the aqueous Zn battery shows a specific energy of ≈144 Wh kg^{-1} at 0.3 A g^{-1}. Meanwhile, it can maintain an energy density of 90 Wh kg^{-1} at a high power density of 6.4 kW kg^{-1} (based on the cathode and 200% Zn anode), making it a promising candidate for high-performance, low-cost, safe, and environment-friendly energy-storage devices.

Large-scale energy storage systems are critical for the integration of renewable energy and electric energy infrastructures.[1–3] Among numerous candidates, lithium-ion batteries with organic electrolytes are one of the most attractive options due to their high energy density[4–10] and mature markets.[11,12] However, for grid scale energy storage, the cost of lithium-ion batteries is still too high,[13,14] and the use of the flammable organic electrolyte in large format batteries poses a severe safety and environmental concern.[15] As an alternative, low-cost aqueous batteries with earth abundant elements as the charge carriers, including Na^+ and Zn^{2+}, are more promising.[16–21]

Among the aqueous rechargeable batteries, Zn^{2+}-based batteries exhibit a series of unique attributes for large-scale energy storage: (i) feasibility of using low-cost Zn metal anode with a high theoretical specific capacity of 819 mA h g^{-1}; (ii) replacement of the traditional alkaline electrolytes by mild neutral electrolytes, mitigating the environmental disruption and recycling costs; and (iii) low redox potential of Zn/Zn^{2+} (−0.76 V vs standard hydrogen electrode) and two-electron transfer mechanism during cycling responsible for the high energy density.[6,22,23] However, the zinc system also has long-standing challenges, such as the unstable cathode and anode structures in the aqueous environment.

On the cathode side, the cycling stability is related to how zinc ions and the electrolyte react with the cathode materials, which is much more complex as compared to the lithium-ion systems. An initial attempt on the hexacyanoferrate system delivered a limited capacity (≈60 mA h g^{-1}), although a high operation voltage of ≈1.7 V was achieved.[23–28] Recently, Pan et al. demonstrated that the manganese oxide cathode goes through a chemical conversion reaction with the zinc species and H_2O rather than the simple intercalation process, delivering a high capacity of ≈285 mA h g^{-1} and an operating voltage of ≈1.44 V.[29] Nazar's group developed a $Zn_{0.25}V_2O_5 \cdot nH_2O$ cathode material, which displayed a specific energy of ≈250 Wh kg^{-1} (based on cathode) and a high capacity of 220 mA h g^{-1} at 15 C (1 C = 300 mA g^{-1}).[30] During cycling, the structural water in $Zn_{0.25}V_2O_5 \cdot nH_2O$ was revealed to exchange with Zn^{2+} reversibly, thus resulting in good kinetics and rate performance. Furthermore, some other studies have also suggested the importance of H_2O in metal ion intercalation.[23,31] During cycling, the solvating H_2O works as a charge shield for the metal ions (Al^{3+}, Mg^{2+}, Li^+, etc.), reducing their effective charges and hence their interactions with the host frameworks.[32,33] This strategy has been investigated to enhance the capacity and rate capability of Li^+, Na^+, and Mg^{2+} batteries.[34–39]

In this paper, we present a systematic and detailed study of the role of H_2O in bilayer $V_2O_5 \cdot nH_2O$ ($n \geq 1$) as a prototype cathode material for zinc batteries. By coupling the electrochemical measurements, thermogravimetric/differential
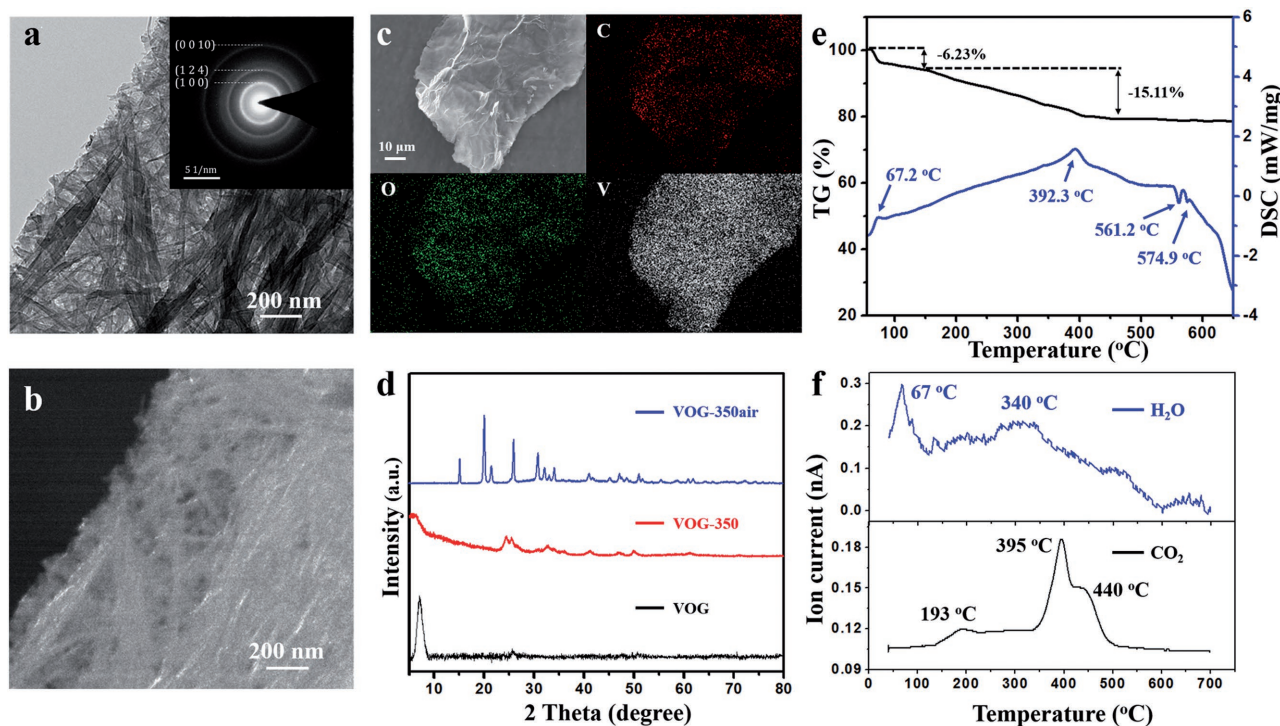
Dr. M. Yan, Dr. S. Wang, Prof. J. Yang
Materials Science and Engineering Department
University of Washington
Seattle, WA 98195-2120, USA
E-mail: jihuiy@uw.edu
Dr. M. Yan, P. He, Dr. Q. Wei, K. Zhao, Dr. X. Xu,
Prof. Q. An, Y. Shuang, Prof. L. Mai
State Key Laboratory of Advanced Technology
for Materials Synthesis and Processing
Wuhan University of Technology
Wuhan 430070, China
E-mail: mlq518@whut.edu.cn
Dr. Y. Chen, Dr. Y. Shao, Dr. K. T. Mueller, Dr. J. Liu
Pacific Northwest National Laboratory
Richland, WA 99352, USA

**ADVANCED
SCIENCE NEWS**

www.advancedsciencenews.com

**ADVANCED
MATERIALS**

www.advmat.de

Figure 1. a,b) The bright-field TEM image with selected area electron diffraction pattern, and (1 0 0) dark-field TEM image. c) EDS elemental mappings of the as-prepared VOG. d) Powder XRD patterns of VOG, VOG-350, and VOG-350air. e,f) TG/DSC-MS results of VOG.

scanning calorimetric-mass spectrometric (TG/DSC-MS) tests, solid-state nuclear magnetic resonance (NMR) spectroscopy, and X-ray diffraction (XRD) analyses, we provide direct evidence on how H_2O participates in the zinc-ion (de)intercalation processes in each step. These water molecules effectively function like a "lubricant" to facilitate fast zinc-ion transport and improve electrochemical performance. As a result, the aqueous Zn battery system displays a specific energy of 144 Wh kg^{-1}, a capacity of 295 mA h g^{-1} at a power density of 6.4 kW kg^{-1} (based on the cathode and 200% Zn anode).

$V_2O_5 \cdot nH_2O$/graphene (VOG) was synthesized using a liquid phase method (see Experimental Section). Transmission electron microscopy (TEM) and scanning electron microscopy (SEM) were employed to characterize the morphology of as-prepared VOG. The VOG displays a plate-like structure (Figure S1, Supporting Information). The highly interconnected vanadium oxide nanowires framework is supported by reduced graphene oxide (**Figure 1**a,b). The selected area electron diffraction pattern shows three diffraction rings, corresponding to the (1 0 0), (1 2 4), and (0 0 10) planes of the polycrystalline bilayer V_2O_5. Energy-dispersive X-ray spectrometer (EDS) elemental mappings of the as-prepared VOG show that the V, O, and C elements are homogeneously distributed in the sample (Figure 1c). Subsequently, TG/DSC-MS was used to investigate the water content. Figure 1e,f shows ≈6.23% weight loss up to ≈100 °C, which is mainly attributed to the physically absorbed water. Additional weight loss of 15.11% appears from 150 to 500 °C, primarily due to the loss of structural water (≈340 °C), the burning of graphene oxides in the composite (≈395 and ≈440 °C), and the non-anchored vanadium oxide (≈193 °C). Thus, the sample annealed at 350 °C was chosen as the control

sample, in which most of the graphene oxides were intact without the structural water. Based on the weight losses attributed to the physically absorbed water and structural water, we estimated that there are 1.29 structural water in each formula unit of VOG. The main XRD peak of VOG shows a large interlayer spacing of ≈12.6 Å (Figure 1d), consistent with the recent reports on bilayer V_2O_5.[40–42] After heat treatment at 350 °C in vacuum for 2 h (VOG-350, without structural water), the peak corresponding to the interlayer spacing of 12.6 Å disappears. The triclinic phase (space group *P1*) was further refined by the Rietveld method with TOPAS 5.0. The lattice parameters were calculated to be $a = 3.271(7)$ Å, $b = 11.696(8)$ Å, $c = 11.072(5)$ Å, $\alpha = 88.645(7)°$, and $\beta = 87.378(0)°$ with satisfactory convergence factors GOF = 1.16, $R_{wp} = 8.45\%$, and $R_p = 6.10\%$ (Figure S2, Supporting Information). As shown in Figure 1d and Figure S3 in the Supporting Information, an orthorhombic V_2O_5 with a space group of *Pmmn* is obtained if annealing VOG at 350 °C in air for 2 h (VOG-350air). As demonstrated by the EDS data (Figures S4 and S5, Supporting Information), the graphene oxides are well kept in both VOG-350 and VOG-350air. No obvious separation between graphene oxide and vanadium oxide is observed. To further investigate the role of structural water in the electrochemical storage processes, VOG and VOG-350 were used for the subsequent electrochemical measurements.

The slurry of electrode was prepared by mixing active materials, conductive carbon (Super-P, 99+%), and polyvinylidene fluoride with the mass ratio of 7: 2: 1, respectively. Then, the slurry was cast onto a Ti foil with a mass loading of ≈2.5 mg cm^{-2}. The electrochemical performance was tested using coin cells with 3 mol L^{-1} Zn(CF$_3$SO$_3$)$_2$ as the electrolyte and Zn foil as

**ADVANCED
SCIENCE NEWS**
www.advancedsciencenews.com

**ADVANCED
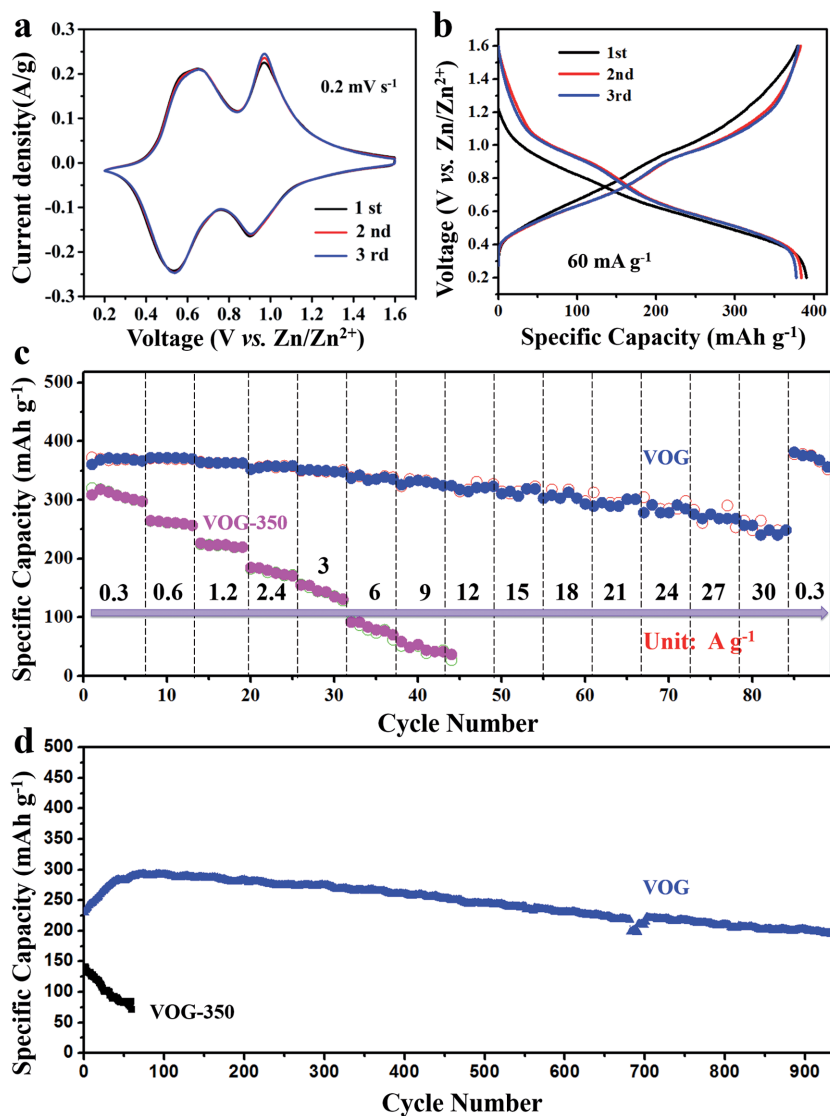MATERIALS**
www.advmat.de

Figure 2. a) CV and b) charge–discharge curves for the first three cycles of the as-prepared VOG. c) Rate capability of VOG and VOG-350 at various current densities. d) Cycling performance of VOG and VOG-350 at 6 A g⁻¹.

good crystal structure stability and reversibility of the redox reactions. The cycle life at 6 A g⁻¹ was further investigated (Figure 2d). The cycling performance of VOG indicates that a 71% of the maximum capacity is achieved after 900 cycles. The initial increase in capacity for the first 50 cycles might be attributed to the activation of bilayer V_2O_5 at a high current density of 6 A g⁻¹. For the control experiment, VOG-350 (without structural water) displays a much poorer rate and cycling performance than those of VOG. At a current density of 6 A g⁻¹, VOG-350 only shows an initial capacity of ≈157 mA h g⁻¹, which further decreases to ≈78 mA h g⁻¹ after 50 cycles.

To further understand the greatly enhanced Zn-ion cycle stability and storage performance, the electrochemical kinetics of VOG was studied in details. If one assumes that the current of CV obeys an empirical power-law relationship with the scan rate

$$i = av^b \tag{1}$$

where i is current, v is scan rate, and a and b are adjustable parameters. **Figure 3**a shows CV curves of VOG at different scanning rates. The b values of peaks 1–4 are found to be 1.03, 0.85, 0.86, and 0.81. This implies that the corresponding redox reactions at the peak regions are mainly limited by the chemical reaction rate rather than the ion diffusion speed within the scanning rate ranging from 0.1 to 1 mV s⁻¹.[43] The high energy and high power densities of VOG are further evident in the Ragone plot, in comparison to α-MnO_2 and $Zn_{0.25}V_2O_5 \cdot nH_2O$.[29,30] VOG exhibits the highest energy density of the three while limiting the discharge time within 1 h, and delivers high energy densities over the power densities from 10^2 to 10^4 W kg⁻¹. As shown in Figure 3d, VOG can achieve an energy density of ≈290 Wh kg⁻¹ at 60 mA g⁻¹ and maintains at ≈171 Wh kg⁻¹ with a power density of 12.2 kW kg⁻¹.

XRD was used to investigate the evolution of crystal structure as a function of the Zn^{2+} content. As shown in **Figure 4**a, the crystal structure of VOG is fully reversible during the intercalation and extraction of Zn ions. During the charging process, Zn ions are extracted from the interlayer, and the interlayer spacing of bilayer V_2O_5 changes from 12.6 to 10.4 Å after charging to 1.3 V (Figure S7, Supporting Information). For the discharge process, the first discharge redox appears at ≈1.1 V and ends at ≈0.8 V. About 0.3 mol Zn ion is intercalated into the layer without phase transformation when discharged from 1.1 to 0.8 V (calculated from the capacity of battery). The second discharge redox happens with the voltage range of 0.6–0.4 V, and a dramatic change in XRD paterns is observed during this period. It is found that a series of new peaks located at 6.53°, 13.14°,
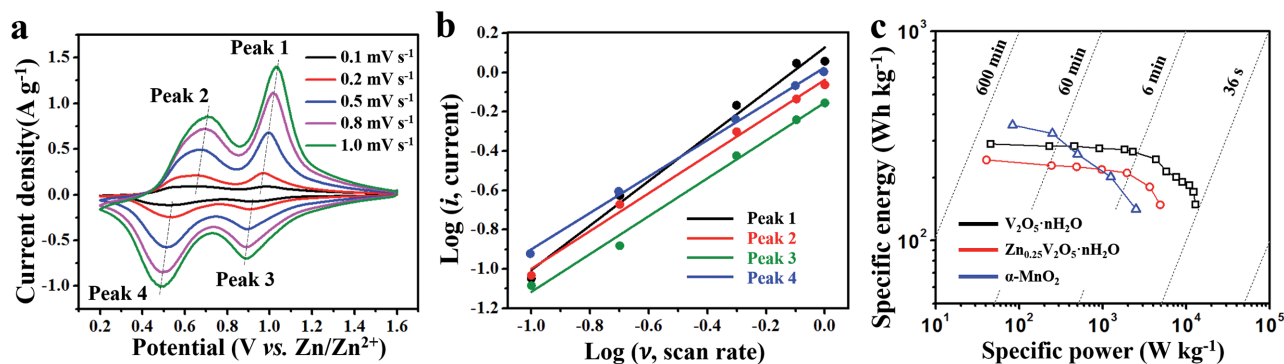
the anodes. **Figure 2**a displays the cyclic voltammetry (CV) of VOG electrode between 0.2 and 1.6 V versus Zn/Zn^{2+} at a scan rate of 0.2 mV s⁻¹. There are two pairs of redox peaks located at 0.97/0.91 V and 0.63/0.54 V. The overlapping of CV curves of the initial three cycles indicates excellent reversibility of Zn^{2+} intercalation/deintercalation reactions that is further verified by the almost reversible initial three cycles at 60 mA g⁻¹. As shown in Figure 2b, a high initial capacity of 381 mA h g⁻¹ is achieved. The two distinct sloping discharge/charge profiles suggest two solid-solution reaction processes associated with Zn-ion intercalation/deintercalation. In particular, the specific capacity (Figure S6, Supporting Information) only decreases ≈14% when the current density increases from 0.3 (372 mA h g⁻¹) to 15 A g⁻¹ (319 mA h g⁻¹). Even at a high rate of 30 A g⁻¹, a discharge capacity of 248 mA h g⁻¹ can still be delivered. Meanwhile, an average capacity of 369 mA h g⁻¹ is retained after over 80 cycles at various current densities (Figure 2c), indicating

**ADVANCED
SCIENCE NEWS**
www.advancedsciencenews.com

**ADVANCED
MATERIALS**
www.advmat.de

Figure 3. a) CV curves of VOG at different scan rates of 0.1, 0.2, 0.5, 0.8, and 1.0 mV s^{-1}. b) log(i) versus log(v) plots of the cathodic current response at four peaks shown in (a). The slopes of this line determine b values. c) Comparison of the Ragone plot between the $V_2O_5 \cdot H_2O$ cell and two other reported materials for aqueous Zn batteries.[29,30] In this figure, the energy density values were calculated by integrating the voltage profile during discharge.

and 19.73° appear when discharged to 0.4 V, corresponding to the interlayer distances of 13.5, 6.7, and 4.5 Å, respectively (Figure S8, Supporting Information). This indicates that a new phase with the interlayer distance of 13.5 Å is formed, due to the intercalation of Zn ions. Thus, two phases coexist at 0.4 V. Based on the result of Rietveld refinement, the first phase is similar to that of VOG charged to 1.3 V. The other is a newly formed phase with the space group of *Pc*. The XRD pattern of the newly formed phase is further extracted from that of VOG discharged to 0.4 V. As shown in Figure S9 (Supporting Information), the peaks located at 13.14° and 19.73° are indexed as the high-order diffraction of that at 6.53°. This phenomenon is different from the XRD results of $Zn_{0.25}V_2O_5$ under operando conditions,[30] in which the lattice interlayer distance decreases with Zn^{2+} intercalation. For VOG, the interlayer distance increases from 10.4 to 13.5 Å upon Zn^{2+} intercalation, in contrast to the previously reported lattice contraction, which we attribute to the coexistence of structural water and Zn^{2+} in between V_2O_5 bilayers. The water-based shielding layer reduces the "effective charge" of Zn^{2+}; meanwhile, it also increases the distance between Zn^{2+} and the neighboring oxygen ions (r_0).

It is well known that the electrostatic bond strength is $\propto \frac{1}{\varepsilon_r r_0^2}$, where ε_r is the permittivity of water and r_0 the distance between Zn^{2+} and the closest ions. Thus, the water-based shielding layer results in the reduced electrostatic bond strength, which is the ultimate reason for three times higher diffusion coefficient of solvated Zn^{2+} and thus the high power density of VOG (Figure S10, Supporting Information).

Solid-state magic-angle-spinning (MAS) NMR is used to further explore structure evolution and the effect of structural water in the electrode materials (Figure 4b). Because physically absorbed water has been removed before the NMR measurements, the broad resonance at 5.6 ppm shown in the ^1H spectrum of pristine VOG (black line) is attributed to the structural water trapped in between V_2O_5 bilayers. After dipping VOG in the electrolyte and charged to 1.3 V, ^1H peak (blue lines) shifts slightly upward to 5.3 ppm with an increased signal intensity, corresponding to 1.8 H_2O per formula unit of VOG (after normalizing to the weight of active materials packed in rotors). Meanwhile, the quartet at 120 ppm in the ^{13}C spectrum and the resonance at −80 ppm in the ^{19}F spectrum both manifest

the existence of anion $CF_3SO_3^-$ in VOG at 1.3 V. The intercalation of water and electrolyte ions ($CF_3SO_3^-$ and Zn^{2+} together to maintain charge balance), indicated by the simultaneous gain in the ^1H, ^{13}C, and ^{19}F signals, is accompanied with the decrease in the VOG interlayer distance from 12.6 to 10.4 Å while maintaining the voltage at 1.3 V. This can be explained by the formation of hydrogen bonds among Zn^{2+}, $CF_3SO_3^-$, H_2O, and lattice oxygen that pulls VOG bilayers closer (Figure 4c).[44] The hypothesis is supported by the dramatic change in proton spin-lattice relaxation time T_1 (Figure S11, Supporting Information) from a single-component 6 ms in pristine VOG to a clear two-component decay with 10 ms (30%) and 3 s (70%). The much longer T_1 component at the slow motion regime implies that 1.3 mol H_2O molecules per unit VOG experience a much more rigid environment and much slower motion at a interlayer distance of 10.4 Å. After discharging to 0.2 V, ^1H resonance (red lines) splits into a relatively sharp peak at 5.1 ppm, which contributes to 20% of the total signal (corresponding to 0.2 mol H_2O per unit VOG from quantitative analysis) and a relatively broad peak at 2.9 ppm (1 mol H_2O per unit VOG). We assign the broad peak to the water molecules associated with 1.2 mol Zn (calculated from battery capacity) incorporated into VOG during discharge. The sharp peak is attributed to water molecules in the few remaining clusters of Zn^{2+}, $CF_3SO_3^-$, and H_2O; its narrow linewidth can be explained by the relatively higher mobility as a result of the increased bilayer distance from 10.4 to 13.5 Å (Figure 4c). This assignment is further corroborated by the significant decrease in the ^{13}C and ^{19}F signal, which indicates that only 1/5 of $CF_3SO_3^-$ is remained after discharging to 0.2 V. The two additional broader resonances at −56 and −91 ppm in the ^{19}F spectrum and the additional peak at 43 ppm in the ^{13}C spectrum are ascribed to the breakdown products of $CF_3SO_3^-$ and their sequential interactions with the VOG lattice. Based on these data and discussion, it is clear that water is highly involved in the battery charge/discharge processes and plays an important role in the battery performance.

In conclusion, our aqueous Zn battery system based on $V_2O_5 \cdot nH_2O$ shows an energy density of 144 Wh kg^{-1} (based on the cathode and 200% Zn anode) and retains the high energy densities over the power densities from 10^2 to 10^4 W kg^{-1}. The structural evolution characterization and electrochemical

**ADVANCED
SCIENCE NEWS**
www.advancedsciencenews.com
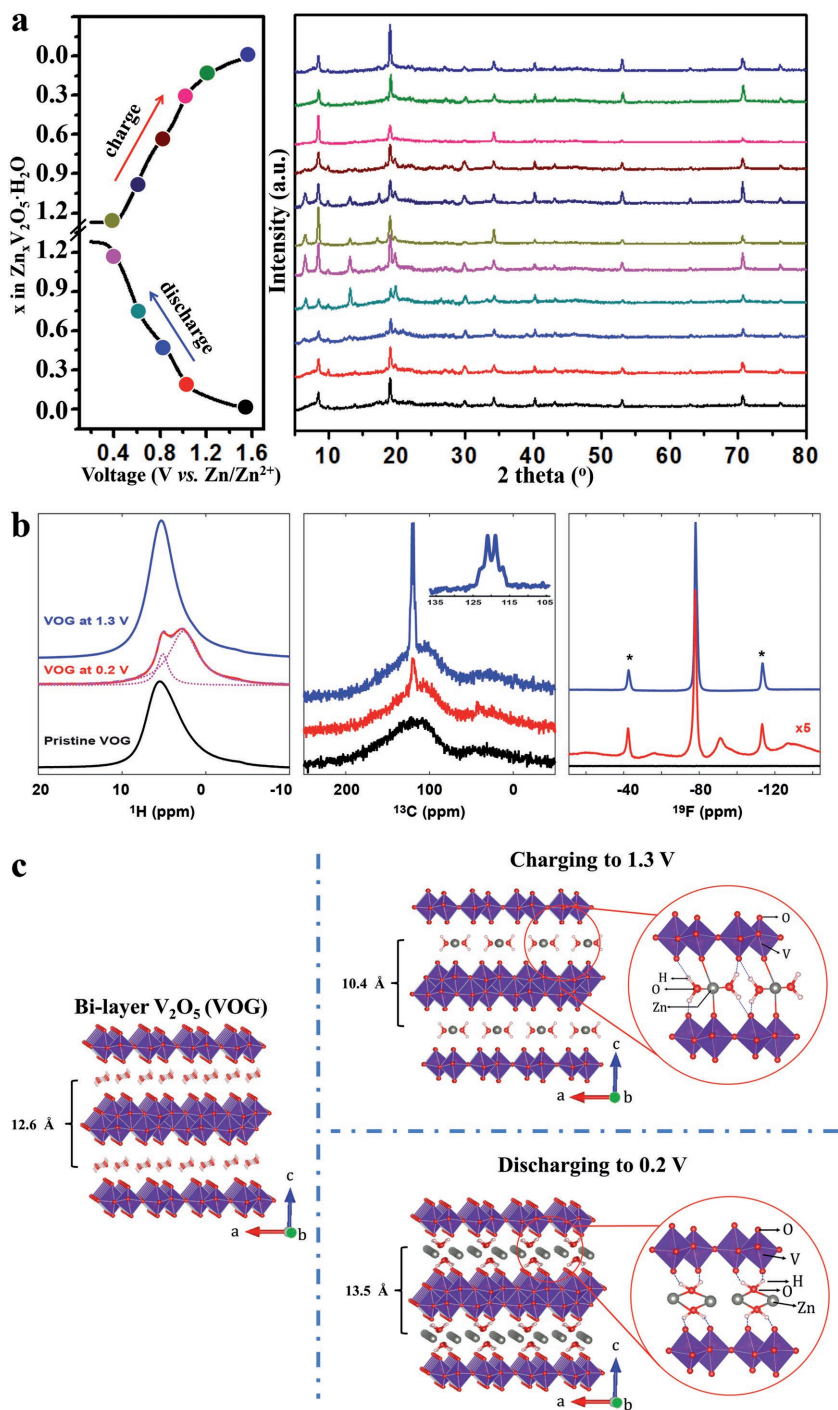
**ADVANCED
MATERIALS**
www.advmat.de

Figure 4. a) XRD study of VOG at different charge and discharge states. The corresponding positions of the XRD patterns are labeled with the same colors of the charge/discharge curve. b) MAS NMR spectra collected for pristine VOG (black line), VOG after charging to 1.3 V (blue line), and discharging to 0.2 V (red line). Deconvolution of the ^1H spectrum of VOG at 0.2 V (pink dot lines) shows that the sharp peak at 5.1 ppm contributes to 20% of the total signal. The spinning speed is 30 kHz for ^1H and ^{13}C, and 20 kHz for ^{19}F with spinning side bands marked with *. c) The proposed crystal structures of pristine VOG, VOG after charging to 1.3 V, and discharging to 0.2 V.

kinetic analyses for the charge–discharge processes demonstrate that the structural water can work as a charge screening media in the redox reactions, increasing the interlayer distance and

decreasing the effective charge of Zn^{2+} by solvation. With comparable energy density to $LiCoO_2$/graphite batteries, the new Zn battery achieves 30 times higher power density, making it a high-performance, low-cost, safe, and environment-friendly energy storage device.

Experimental Section

Synthesis of $V_2O_5 \cdot H_2O$/Graphene: In a typical procedure, 1 mol V_2O_5 sols was mixed with 20 mL reduced graphene oxide solution (0.5 mg mL^{-1}) and stirred for 1 h. Then, 3 mmol $NH_4H_2PO_4$ was added to provide positive charges for the V_2O_5 sols and reduced graphene oxide, which self-assemble due to the electrostatic interactions. Next, the sample was stirred at 80 °C for 6 h. The hydrogels were washed with water to remove the $NH_4H_2PO_4$ after aging at 20 °C for 2 h. The $V_2O_5 \cdot H_2O$/graphene was obtained after frozen-drying for 24 h. The VOG-350 was prepared by annealing $V_2O_5 \cdot H_2O$/graphene at 350 °C for 2 h in vacuum.

Electrochemical Characterization: The electrode was prepared by mixing active material (70 wt%), conductive carbon (Super-P, 20 wt%), and polyvinylidene fluoride (PVDF, 10 wt%), and then the slurry was cast onto a Ti foil and dried in a vacuum oven at 60 °C for 8 h. Zinc foil and glass fiber membrane were used as the anode and separator, respectively, and 3 M zinc trifluoromethanesulfonate aqueous solution was used as the electrolyte. Vanadium sol (0.1 M) was added into the electrolyte to suppress the dissolving of vanadium oxide. CR2016-type coin cells were assembled in air to evaluate the electrochemical performance with a LAND battery testing system (CT2001A). The weight of both graphene and vanadium oxide was considered for calculating the capacity. Cyclic voltammograms were collected on a CHI600E electrochemical workstation. All tests were performed at room temperature.

Materials Characterization: The as-prepared samples were characterized by powder XRD, field emission SEM, TEM, thermogravimetric/differential scanning calorimetric-mass spectrometry (Netzsch STA449F3; Netzsch QMS403C), EDS, and NMR. The field emission SEM images were collected with a JEOL JSM-7100F at an acceleration voltage of 10 kV. EDS of the samples was tested by an Oxford IE250 under 30 kV accelerating voltage with 10 nA beam current. A JEM 2100F field emission TEM (JEOL) working at 200 kV was used to acquire TEM and HR-TEM images in a scanning TEM mode. The as-prepared samples were characterized by powder XRD on a Bruker D8 Advance X-ray diffractometer with Cu Kα radiation ($\lambda = 1.54060$ Å), 280 mm goniometer radius, and range of 5°–80° 2θ. A LYNXEYE XE-T energy dispersive 1D X-ray detector with PSD opening of 2.946° was used to avoid the influences of fluorescence effect. The XRD patterns were obtained at a step scan of 0.006°, a step time of 0.2 s, and a sample rotation speed of 15.00° min^{-1}. ^1H and ^{13}C MAS NMR were performed on a Varian Inova spectrometer with a 600 MHz (14.1 T) magnet, using 1.6 mm rotors operating at a spinning speed of 30 kHz. ^{19}F MAS NMR spectra were collected on a Bruker Avance III spectrometer

also with a 600 MHz (14.1 T) magnet, using 3.2 mm rotors spinning at 20 kHz. The 90° pulse width was 5 µs for ^1H, 2 µs for ^{13}C, and 4 µs for ^{19}F. The ^1H and ^{19}F spectra were obtained with 32 and 256 scans, respectively, using a recycling delay of 30 s for quantitative comparison. Due to the low sensitivity of ^{13}C in the natural abundant materials, 16 000 scans were used with 45° pulse and a recycling delay of 5 s. Proton T_1 was measured using inversion-recovery method. Temperature was maintained at 30 °C for all NMR measurements. Before the NMR measurements, all rotors packed with samples with an open end were placed in an oven at 50 °C for 2 h to eliminate physically absorbed water.

Conflict of Interest

The authors declare no conflict of interest.

[1] L. Mai, L. Xu, C. Han, X. Xu, Y. Luo, S. Zhao, Y. Zhao, *Nano Lett.* **2010**, *10*, 4750.
[2] D. Larcher, J.-M. Tarascon, *Nat. Chem.* **2015**, *7*, 19.
[3] Z. Yang, J. Zhang, M. C. Kintner-Meyer, X. Lu, D. Choi, J. P. Lemmon, J. Liu, *Chem. Rev.* **2011**, *111*, 3577.
[4] M. Yan, F. Wang, C. Han, X. Ma, X. Xu, Q. An, L. Xu, C. Niu, Y. Zhao, X. Tian, *J. Am. Chem. Soc.* **2013**, *135*, 18176.
[5] Y.-K. Sun, Z. Chen, H.-J. Noh, D.-J. Lee, H.-G. Jung, Y. Ren, S. Wang, C. Yoon, S.-T. Myung, K. Amine, *Nat. Mater.* **2012**, *11*, 942.
[6] X. G. Zhang, *Corrosion and Electrochemistry of Zinc*, Springer, New York City, NY, USA **1996**.
[7] M. Sathiya, G. Rousse, K. Ramesha, C. Laisa, H. Vezin, M. T. Sougrati, M.-L. Doublet, D. Foix, D. Gonbeau, W. Walker, *Nat. Mater.* **2013**, *12*, 827.
[8] M. Sathiya, A. M. Abakumov, D. Foix, G. Rousse, K. Ramesha, M. Saubanère, M. Doublet, H. Vezin, C. Laisa, A. Prakash, *Nat. Mater.* **2015**, *14*, 230.
[9] M. Winter, J. O. Besenhard, M. E. Spahr, P. Novák, *Adv. Mater.* **1998**, *10*, 725.
[10] T. Kennedy, M. Brandon, K. M. Ryan, *Adv. Mater.* **2016**, *28*, 5696.
[11] M. Yan, G. Zhang, Q. Wei, X. Tian, K. Zhao, Q. An, L. Zhou, Y. Zhao, C. Niu, W. Ren, *Nano Energy* **2016**, *22*, 406.
[12] J. Liu, J. G. Zhang, Z. Yang, J. P. Lemmon, C. Imhoff, G. L. Graff, L. Li, J. Hu, C. Wang, J. Xiao, *Adv. Funct. Mater.* **2013**, *23*, 929.
[13] T. C. Wanger, *Conserv. Lett.* **2011**, *4*, 202.
[14] E. C. Evarts, *Nature* **2015**, *526*, S93.
[15] E. P. Roth, C. J. Orendorff, *Electrochem. Soc. Interface* **2012**, *21*, 45.
[16] W. Li, J. R. Dahn, D. S. Wainwright, *Science* **1994**, *264*, 1115.
[17] Y. Lu, J. B. Goodenough, Y. Kim, *J. Am. Chem. Soc.* **2011**, *133*, 5756.
[18] J.-Y. Luo, W.-J. Cui, P. He, Y.-Y. Xia, *Nat. Chem.* **2010**, *2*, 760.
[19] J. Y. Luo, Y. Y. Xia, *Adv. Funct. Mater.* **2007**, *17*, 3877.
[20] C. D. Wessells, R. A. Huggins, Y. Cui, *Nat. Commun.* **2011**, *2*, 550.
[21] M. Pasta, C. D. Wessells, R. A. Huggins, Y. Cui, *Nat. Commun.* **2012**, *3*, 1149.
[22] M. Chamoun, B. J. Hertzberg, T. Gupta, D. Davies, S. Bhadra, B. Van Tassell, C. Erdonmez, D. A. Steingart, *NPG Asia Mater.* **2015**, *7*, e178.
[23] L. Zhang, L. Chen, X. Zhou, Z. Liu, *Adv. Energy Mater.* **2015**, *5*, 1400930.
[24] R. Trócoli, F. La Mantia, *ChemSusChem* **2015**, *8*, 481.
[25] Z. Jia, B. Wang, Y. Wang, *Mater. Chem. Phys.* **2015**, *149*, 601.
[26] M. S. Chae, J. W. Heo, H. H. Kwak, H. Lee, S.-T. Hong, *J. Power Sources* **2017**, *337*, 204.
[27] T. Gupta, A. Kim, S. Phadke, S. Biswas, T. Luong, B. J. Hertzberg, M. Chamoun, K. Evans-Lutterodt, D. A. Steingart, *J. Power Sources* **2016**, *305*, 22.
[28] G. Kasiri, R. Trócoli, A. B. Hashemi, F. La Mantia, *Electrochim. Acta* **2016**, *222*, 74.
[29] H. Pan, Y. Shao, P. Yan, Y. Cheng, K. S. Han, Z. Nie, C. Wang, J. Yang, X. Li, P. Bhattacharya, *Nat. Energy* **2016**, *1*, 16039.
[30] D. Kundu, B. D. Adams, V. Duffort, S. H. Vajargah, L. F. Nazar, *Nat. Energy* **2016**, *1*, 16119.
[31] Q. An, Y. Li, H. Yoo, S. Chen, Q. Ru, L. Mai, Y. Yao, *Nano Energy* **2015**, *18*, 265.
[32] P. Novak, J. Desilvestro, *J. Electrochem. Soc.* **1993**, *140*, 140.
[33] E. Levi, Y. Gofer, D. Aurbach, *Chem. Mater.* **2009**, *22*, 860.
[34] K. W. Nam, S. Kim, S. Lee, M. Salama, I. Shterenberg, Y. Gofer, J.-S. Kim, E. Yang, C. S. Park, J.-S. Kim, *Nano Lett.* **2015**, *15*, 4071.
[35] C. Kim, P. J. Phillips, B. Key, T. Yi, D. Nordlund, Y. S. Yu, R. D. Bayliss, S. D. Han, M. He, Z. Zhang, *Adv. Mater.* **2015**, *27*, 3377.
[36] R. Tripathi, T. Ramesh, B. L. Ellis, L. F. Nazar, *Angew. Chem.* **2010**, *122*, 8920.
[37] S. Tepavcevic, H. Xiong, V. R. Stamenkovic, X. Zuo, M. Balasubramanian, V. B. Prakapenka, C. S. Johnson, T. Rajh, *ACS Nano* **2011**, *6*, 530.
[38] Y. Wang, K. Takahashi, K. H. Lee, G. Cao, *Adv. Funct. Mater.* **2006**, *16*, 1133.
[39] M. Naguib, J. Halim, J. Lu, K. M. Cook, L. Hultman, Y. Gogotsi, M. W. Barsoum, *J. Am. Chem. Soc.* **2013**, *135*, 15966.
[40] V. Petkov, P. N. Trikalitis, E. S. Bozin, S. J. Billinge, T. Vogt, M. G. Kanatzidis, *J. Am. Chem. Soc.* **2002**, *124*, 10157.
[41] N. Sa, T. L. Kinnibrugh, H. Wang, G. Sai Gautam, K. W. Chapman, J. T. Vaughey, B. Key, T. T. Fister, J. W. Freeland, D. L. Proffit, *Chem. Mater.* **2016**, *28*, 2962.
[42] D. Su, G. Wang, *ACS Nano* **2013**, *7*, 11218.
[43] H.-S. Kim, J. B. Cook, H. Lin, J. S. Ko, S. H. Tolbert, V. Ozolins, B. Dunn, *Nat. Mater.* **2017**, *16*, 454.
[44] G. G. Sai, P. Canepa, W. D. Richards, R. Malik, G. Ceder, *Nano Lett.* **2016**, 2426.